Hindawi
International Journal of Antennas and Propagation
Volume 2019, Article ID 6463101, 12 pages
https://doi.org/10.1155/2019/6463101

Research Article

A Compact CPW-Fed Low-Profile Wideband Circularly Polarized Slot Antenna with a Planar Ring Reflector for GNSS Applications

Jiade Yuan, Yujie Li, Zhimeng Xu, and Jiamin Zheng

College of Physics and Information Engineering, Fuzhou University, Fuzhou 350116, China

Correspondence should be addressed to Jiade Yuan; yuanjiade@fzu.edu.cn

Received 19 July 2019; Revised 23 September 2019; Accepted 30 September 2019; Published 31 October 2019

Academic Editor: Giorgio Montisci

A compact low-profile wideband circularly polarized slot antenna for global navigation satellite system (GNSS) is presented. The antenna comprises a planar slot radiator with a coplanar waveguide (CPW) feed and a modified ring-shaped reflector to achieve unidirectional radiation. The modified reflector is an inner square patch with four slantly cut corners, a center ring, and an outer ring with a notch; they significantly reduce the separation between the antenna radiator and reflector and therefore the overall antenna height. The overall dimensions are $\lambda_0/3 \times \lambda_0/3 \times \lambda_0/30$ (λ_0 denotes the free space wavelength at lower frequency). The measured −10 dB bandwidth of $|S_{11}|$, 3-dB axial ratio (AR) bandwidth, and maximum gain are of 1.53–2.28 GHz, 1.558–1.672 GHz, and 5.87 dBi, respectively. The proposed antenna is simple without any additional feeding networks or shorting probes.

1. Introduction

Handheld terminals of global navigation satellite system (GNSS) have been popular in emergency communication, such as inshore fishery, emergency rescue, and forest fire prevention. As a key component, the antennas of the terminals not only have to be of small size, low profile, and unidirectional radiation but also must have a wide bandwidth to cover the multiple frequency bands of GNSS, such as GPS L_1 (1575.42 ± 1.023 MHz), BDS B_1 (1561.098 ± 5 MHz), and GLONASS L_1 (1602.5 ± 4 MHz) [1, 2].

Various techniques to broaden antenna bandwidth of unidirectional radiation antenna have been reported. In [3–6], parasitic patches or coupling feed structure is applied to increase bandwidth. The antenna bandwidth is increased using four parasitic strips and a capacitive-coupled feed in [3], using a Γ-shaped coupling feed structure in [4], using a tapped coupling line in [5], and using four feed strips coupling with the slot cavity in [6]. In [7], the broadband of a circularly polarized directional antenna is achieved with a circular radiating patch, a ground plane, and a novel coupling feeding network. The slot antenna's ARBW and IBW cover the frequency band of 75.8% (1.13–2.51 GHz). In [8], a circular polarized antenna with an IBW of 0.900–2.95 GHz and ARBW of 1.0–2.87 GHz is developed. The antenna is composed of two orthogonally placed elliptical dipoles printed on both sides of a substrate. In [9], a novel wideband technique is presented based on the mode analysis and the bandwidth is expanded by loading a folded shorting pin. The operating frequency covers the band of 1.1–1.6 GHz. The antenna has an overall size of only $0.4\ \lambda_0 \times 0.4\ \lambda_0 \times 0.05\ \lambda_0$ when the relative permittivity of the substrate is 6. In [10], the antenna is proposed and has the IBW of 1.02 to 2.18 GHz and ARBW of 1.15 to 2 GHz using four claw-shaped parasitic branches. Although the abovementioned antennas have wide bandwidths and good directional radiation pattern, they have relatively larger size or complicated feeding network. As a result, they are not suitable for uses in handheld devices and for mass production.

In recent years, new antennas of simpler structures that have excellent IBW and ARBW have been reported [11–16]. In [11], a coplanar waveguide- (CPW-) fed square slot antenna is presented where an L-shaped feedline and a rectangle-shaped parasitic element is used to obtain the IBW of 63.97% and ARBW of 48.28%. In [12], by embedding a pair of inverted L-shaped strips and loading two spiral slots

in the ground plane, the high IBW and ARBW of 111% and 56% are achieved, respectively. In [13], instead of using the CPW feed, the microstrip line feed is employed in the slot antenna and a transverse strip is used in the ground plane; they lead to the IBW and ARBW of 90.2% and 40%, respectively. In [14], a horseshoe-shaped slot and two L-shaped radiators are introduced, and the IBW and ARBW are of 113% (0.7–2.52 GHz) and 60.2% (3.47–6.46 GHz), respectively. Although presenting distinct advantages in IBW and ARBW, these antennas have undesirable bidirectional radiation patterns. To obtain a unidirectional radiation pattern, a simple conducting plane is placed underneath the CPW-fed slot antenna without changing its original structural dimensions [16–19]. However, they all need a relatively large distance between the radiators and the conducting planes and fail to meet the requirements of low profile.

In this paper, to overcome the shortcomings of the existing antennas for GNSS systems, we propose the integration of a broadband slot antenna with a modified reflector to form a new compact low-profile antenna that has a wide bandwidth and unidirectional radiation pattern. It has the smallest volume size among the antennas reported so far with an easy and simple coplanar waveguide (CPW) feed. An evolutional approach is presented to show the step-by-step development of the proposed antenna and its operational principles; the approach may also be used for any future developments of new antennas.

2. Configuration and Design of the Proposed Antenna

The cross-sectional view of the proposed slot antenna is shown in Figure 1(a): there are two layers of FR4 substrate separated by air; the radiator and reflector are printed on the upper and lower FR4 substrate layers, respectively.

The top view of the radiator on the upper layer is shown in Figure 1(b). The antenna is fed by a 50 ohm coplanar waveguide (CPW) of a strip width of W_s and the gaps of g_s with the ground. The strip becomes wider as it extends further into the center of the patch with a wider width of W_1. Four grounded rectangular patches with different widths of A_1, W_3, L_2, and A_3 are etched on the top and right sides, respectively. A grounded T-shaped strip with the dimension of L_5, W_5, and W_6 is made on the left side. The geometry of the radiator (Figure 1(b) is evolved from a simple monopole antenna with a grounded loop, as explained in Section 2.1 later. The bottom view of the reflector is shown in Figure 1(c); the reflector comprises of an outer ring, a center ring, and an inner square patch with its four symmetrical corners cut slantly. A notch is etched in the outer ring.

The combination of the radiator placed on the upper layer and the reflector placed on the lower layer forms the proposed low-profile antenna with wide IBW and ARBW. The radiator and reflector should be considered and designed simultaneously because there is strong mutual coupling between them due to a small height h of about $\lambda_o/30$ (Figure 1(a)). In other words, the performance of the radiator is jointly affected by the radiator and the reflector. This is different from the conventional antenna presented in [16–19] where the reflector and the radiator could be designed relatively independently. In addition, through its embedded structures, such as the grounded rectangular patches and the T-shaped strip, the radiator generates orthogonal electric fields, which then lead to the circular polarization with the unidirectional radiation (achieved with the reflector).

The optimized dimensions of the proposed antenna are obtained through simulation using the ANSYS HFSS 18, and the results are listed in Table 1.

2.1. Evolution and the Design Steps of the Proposed Antenna. Six steps (Antennas I–VI) are shown in Figure 2 to explain the evolution and design process of the proposed antenna. The overall size of all the antennas is kept unchanged. The simulated results of $|S_{11}|$, AR at the boresight, and radiation pattern at $f = 1.575$ GHz of Antennas I–VI are presented in Figures 3(a)–3(c), respectively.

Antenna I is a conventional coplanar slot antenna, and the reflector is a square-shaped conducting plane. It has poor performances in $|S_{11}|$, AR, and unidirectional radiation because of the strong influence from the reflector on the radiator. Antenna II is Antenna I with the addition of a ring slot being etched in the reflector; $|S_{11}|$ and the directivity of the radiation pattern become better. The reasons are that the etched slots reduce electromagnetic coupling between the radiator and the reflector and the resulting current distributions improve the impedance matching and unidirectional radiation. Antenna III is Antenna II with an outer ring slot and a notch being etched in the reflector that forms the inner patch, center ring, and outer ring. The notch in the reflector reduces the Q factor due to the close distance between the reflector and the SMA connector on radiator. Antenna III has better directivity than Antenna II because of the introduction of the outer slot that further optimizes the current distribution. From Antenna I to Antenna III, only the reflector is changed and the radiator is symmetric about the central strip of the CPW feed; hence, they lead to linear polarization and high AR values as shown in Figure 3(b).

To achieve the circular polarization and further improve the antenna performance, from Antenna IV to Antenna VI, the radiator is evolved, while the reflector is kept the same. Antenna IV is formed from Antenna III by embedding a T-shaped grounded strip on the left side and a rectangular grounded patch on the top left corner. As a result, the AR performance is improved significantly. The reason is that the transverse electric fields between the inverted T strip and the center strip are excited and its magnitude and phase of the electric field can generate circularly polarized radiation. Antenna V is evolved from Antenna IV by adding a rectangular patch and a stairstep-shaped grounding patches in the right side and lower right corner of the Antenna IV radiator, respectively. As shown in Figures 3(a) and 3(c), $|S_{11}|$ and directivity improve. At last, two rectangular grounding patches are added to the lower left corner and the top of the radiator of Antenna V, respectively; they fine tune

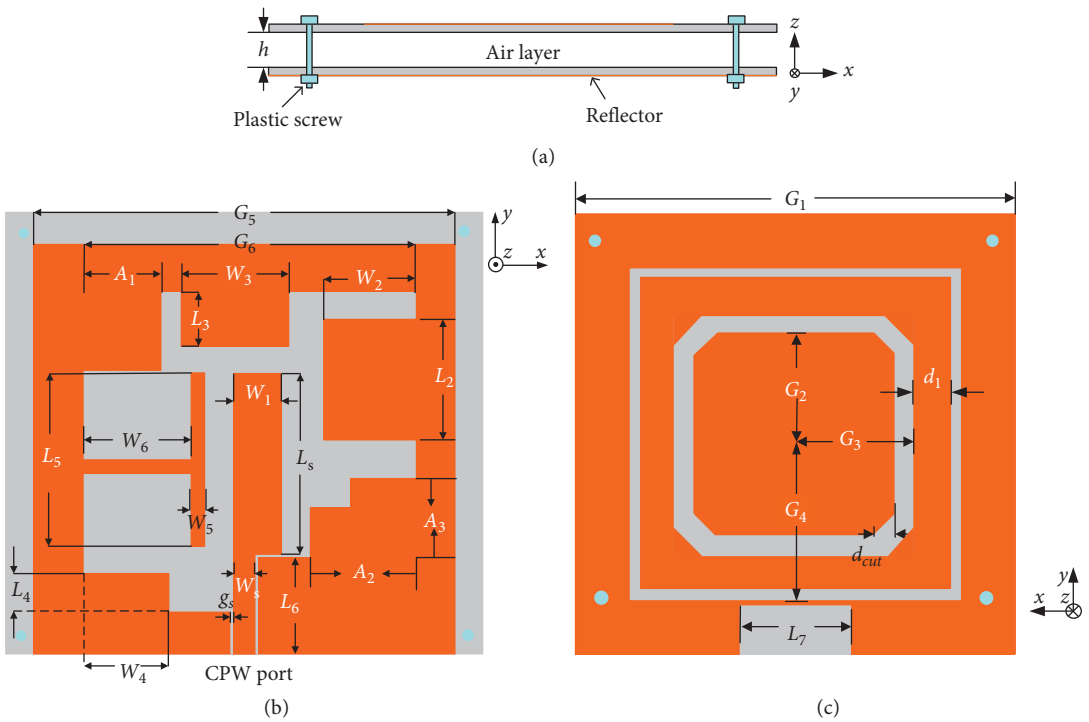

FIGURE 1: The proposed antenna. (a) The cross-sectional view of the antenna, (b) the (top) view of the radiator, and (c) the (bottom) view of the reflector.

TABLE 1: Optimized geometric parameters (unit: mm).

Parm	Value
G_1	65.5
G_2	16
G_3	19
G_4	25.5
G_5	53
G_6	38
d_1	4.5
W_S	3
L_S	21.1
g_s	0.6
d_{cut}	2.2
W_1	6.4
W_2	9
W_3	12
W_4	10
W_5	2
W_6	13
h	5
L_2	14
L_3	7
L_4	4.4
L_5	19
L_6	13.9
L_7	20
A_1	10.4
A_2	11
A_3	10

the antenna performance, and the final design of the antenna VI is formed.

2.2. Generation of Circular Polarization. The current distributions on the radiator at different time instants are simulated and studied as time t increases from $t = 0$ to $t = 270^\circ/\omega = 3T/4$; they are shown in Figure 4 at $f = 1.575$ GHz as a test point.

As seen from Figure 4(a), at $t = 0$, the predominant currents are J_0 on the left and right sides, and they flow in the same $+y$ direction. As seen from Figure 4(b), at the instant of $t = 90^\circ/\omega = T/4$, there are four strong currents: current J_0 on the top and bottom sides that flow in the $-x$ direction, current J_1 on the T-shaped strip that flows in the $-x$ direction, current J_2 on the feed patch that flows in the $+y$ direction, and current J_3 on the rectangular patch adjacent to J_2 that flows in the -y direction. J_2 and J_3 flow in the opposite directions (i.e., $+y$ and $-y$ directions), cancelling the far fields generated by each other; J_0 and J_1 flow in the same direction (i.e., the $-x$ direction), reinforcing the far fields generated by each other. Therefore, at $t = 90^\circ/\omega = T/4$, the predominant currents are in the $-x$ direction.

As further seen from Figures 4(c) and 4(d), the predominant currents at $t = 180^\circ/\omega = T/2$ and $t = 270^\circ/\omega = 3T/4$ are equal in magnitude and opposite in phase to the currents at $t = {}^{0^\circ}/\omega = T/4$ and $t = 90^\circ/\omega = T/2$, respectively.

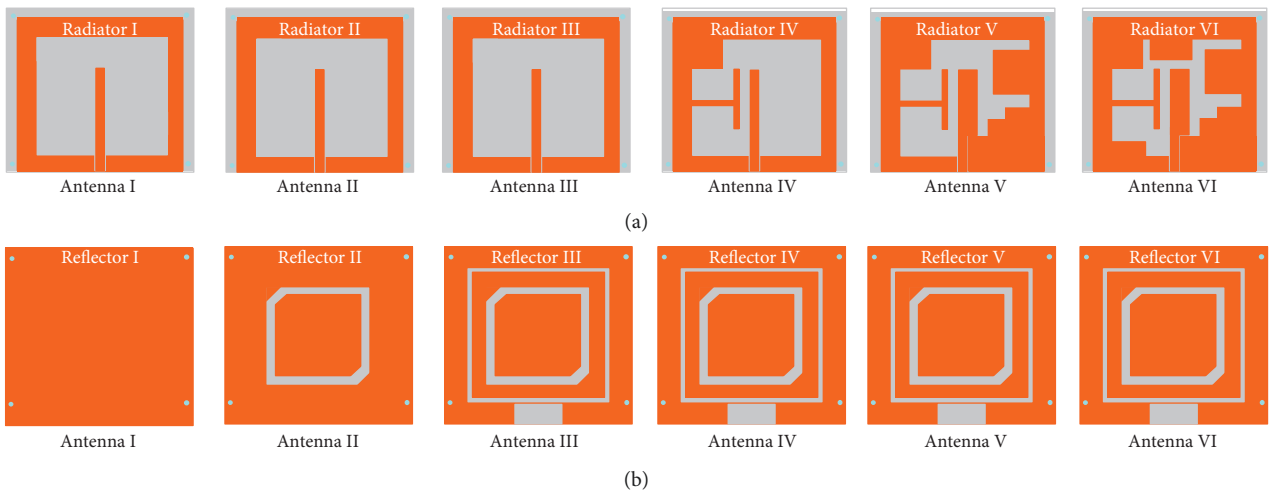

Figure 2: Evolution and the design steps of the proposed antenna, from Antennas I to VI. (a) The radiator on the upper layer and (b) the reflector on the lower layer.

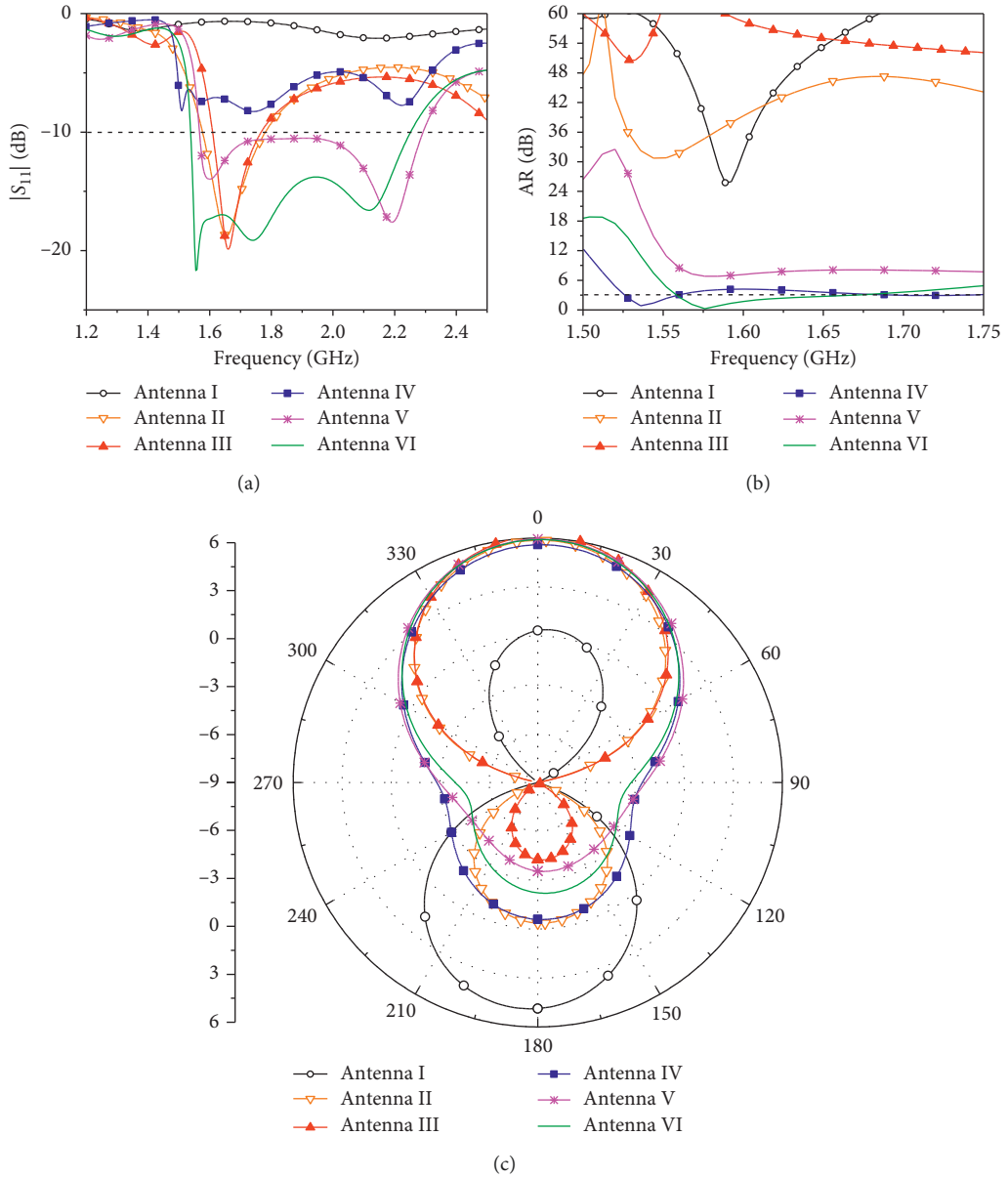

Figure 3: Simulated reflection coefficient $|S_{11}|$ and axial ratio of Antennas I–VI. (a) $|S_{11}|$, (b) axial ration, and (c) radiation pattern.

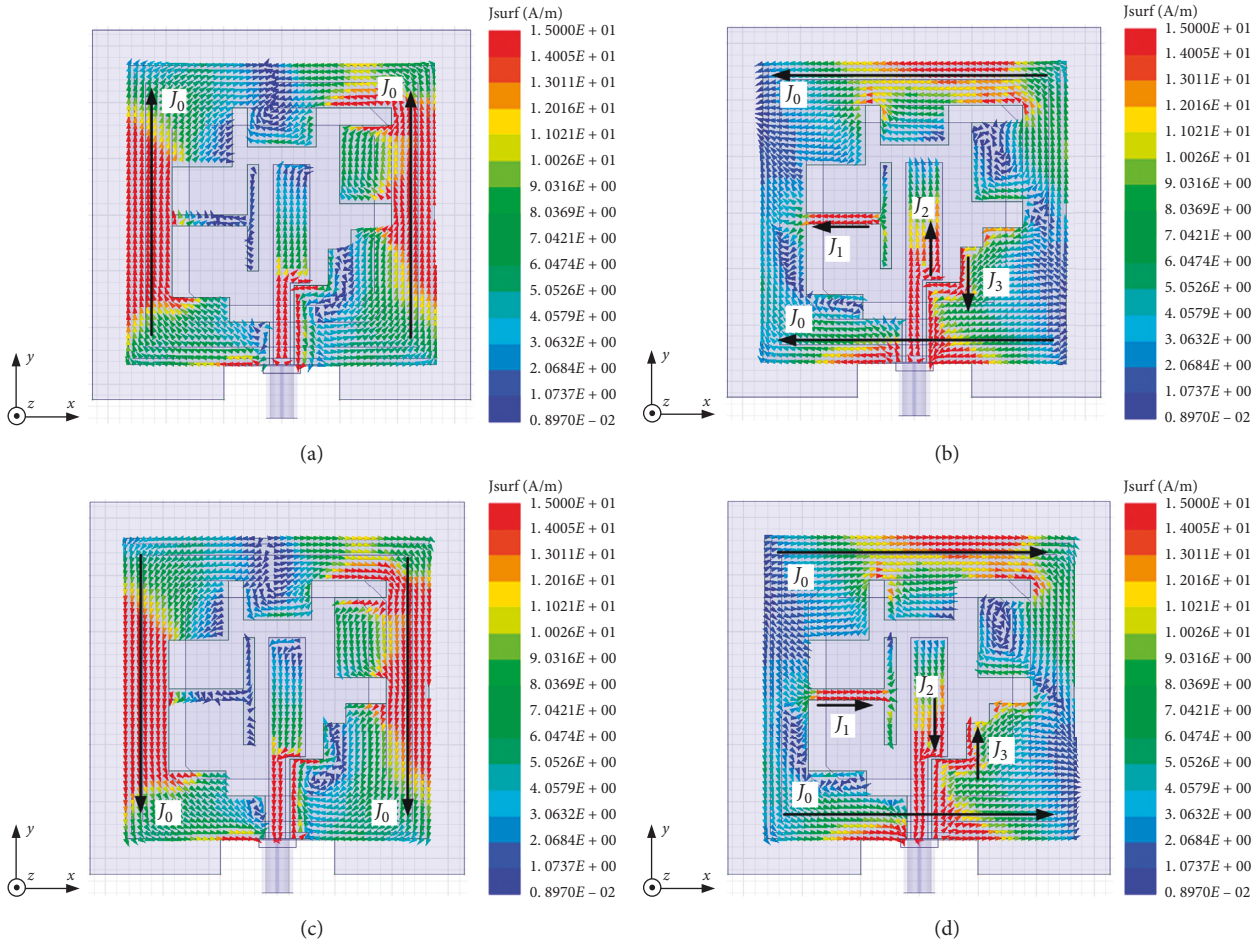

FIGURE 4: Simulated electric current distribution at 1.575 GHz. (a) $t = 0$, (b) $t = T/4$, (c) $t = T/2$, and (d) $t = 3T/4$. T is the period of the sinusoidal fields with angular frequency ω.

Consequently, the vector sum of the predominant currents flows in the anticlockwise direction with time as shown in Figure 4. Such current variations with time result in predominantly a right-hand circular polarization (RHCP) wave radiations in the $z > 0$ half spaces.

3. Parametric Studies

Parametric studies are performed by simulation of the antenna parameters of $|S_{11}|$ and AR; the results allow optimization and final design of the proposed antenna. Unless indicated otherwise, only one geometrical parameter is varied each time, and the rest of the parameters are kept unchanged in the following investigations.

3.1. Dimensions of the Center Strip (or Feedline) (L_s and W_1). $|S_{11}|$ and AR at the boresight of the proposed antenna are affected by the dimensions of the central strip of the CPW feed. Its length and width are denoted as L_s and W_1, respectively. Simulation results are shown in Figures 5(a) and 5(b). When $W_1 = 6.4$ mm and L_s varies from 19.1 mm to 23.1 mm, both $|S_{11}|$ and AR first become better and then worse. When W_1 increases from 4.4 mm to 8.4 mm with fixed $L_s = 21.1$ mm, $|S_{11}|$ has slight variations while AR varies significantly and the frequency of the lowest AR value (in dB) increases. The reason is that W_1 impacts directly the distribution of transverse electric fields in the slots of the radiator and therefore affects the AR. The optimal value is $L_s = 21.1$ mm and $W_1 = 6.4$ mm with the lowest AR of 1.45 dB at the frequency of 1.575 GHz.

3.2. Dimensions of the T-Shaped Strip (W_6 and L_5). $|S_{11}|$ and AR at the boresight of the proposed antenna are affected by the lengths of the ground T-shaped strip, W_6 and L_5. Simulation results are shown in Figures 6(a) and 6(b). When $L_5 = 19$ mm and W_6 increases from 12 mm to 14 mm, $|S_{11}|$ has slight variation while AR shows visible changes. This indicates that AR is more sensitive to W_6; the reason is that the transverse electric field between the T-shaped strip and the center feed strip is sensitive to the gap width (determined by W_6) as it forms the one of the axial polarizations for the circular polarization. For the similar reason, when L_5 increases from 16 mm to 22 mm with the fixed $W_6 = 13$ mm, $|S_{11}|$ varies slightly and AR shows visible variations.

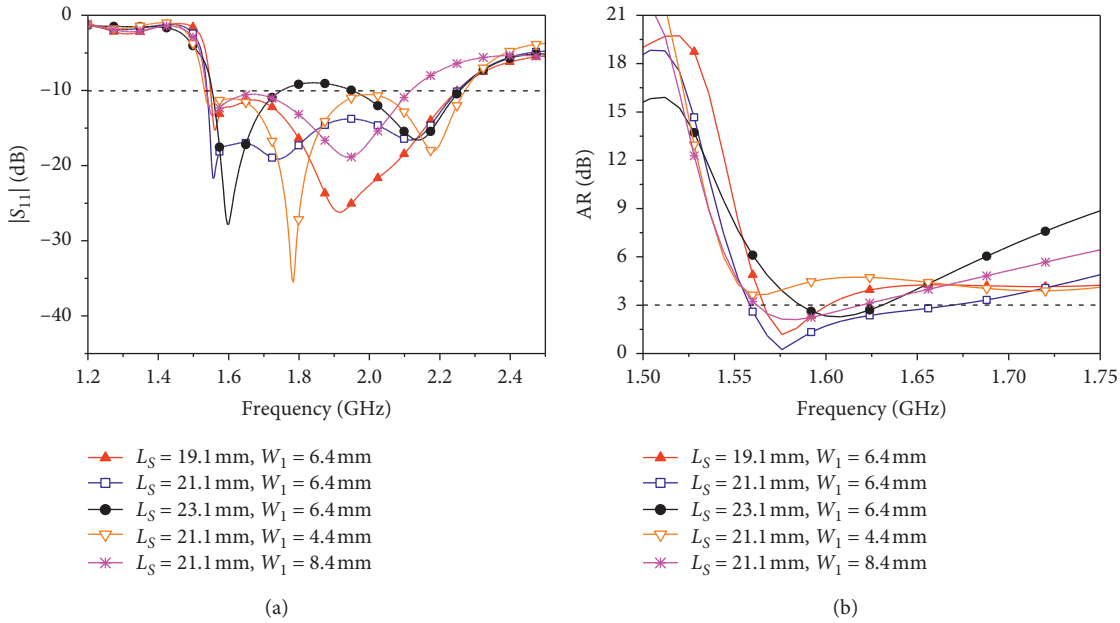

FIGURE 5: Variations of (a) $|S_{11}|$ and (b) AR with different dimensions of center strip, L_s and W_1.

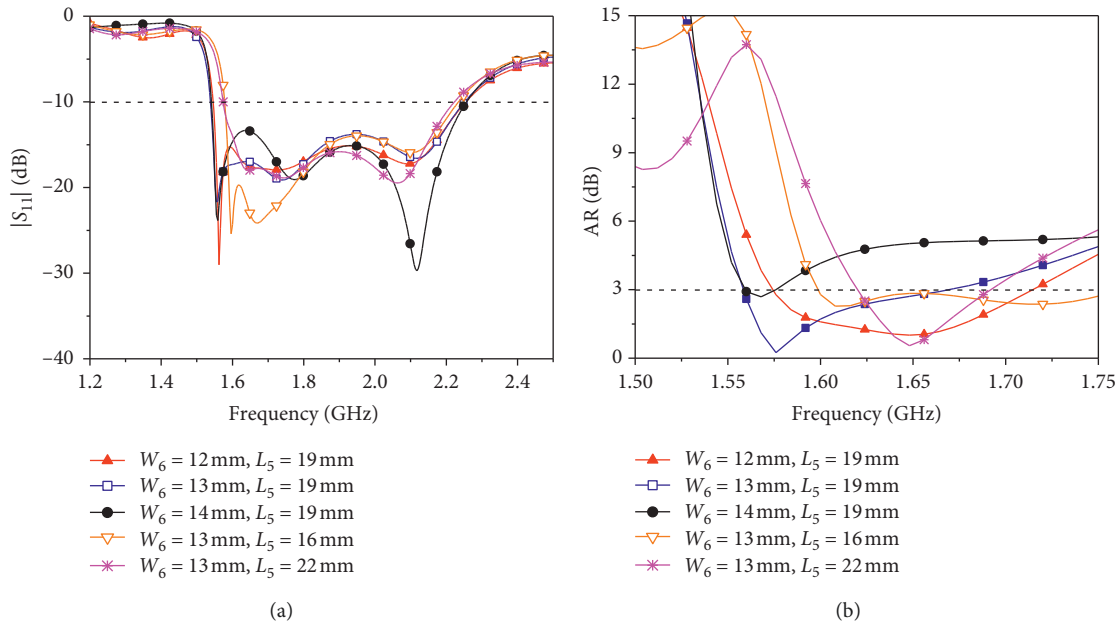

FIGURE 6: Variations of (a) $|S_{11}|$ and (b) AR with different dimensions of the T-shaped strip, W_6 and L_5.

3.3. Dimension of the Inner Square Patches of the Reflector (G_2). Figures 7(a) and 7(b) show the simulation results of $|S_{11}|$ and AR and realized gain of RHCP with the variation of G_2, respectively. It can be observed from Figure 7(a) that the resonant frequency is shifted to the lower value with the increasing of G_2 from 15 mm to 17 mm. The reason can be explained that the equivalent capacitor between the radiator and reflector is increased because the increasing of G_2 means the decreasing of the width of the inner slot of the reflector. Meanwhile, the AR changes to better then worse (see AR curves in Figure 7(b)). The realized gains of RHCP also vary with the increasing of G_2 and appear lower values when $G_2 = 17$ mm, as shown the realized gain curves in Figure 7(b). The main reason is due to the poor AR performance when $G_2 = 17$ mm.

3.4. Dimensions of the Center Ring of the Reflector (G_3 and d_1). G_3 and d_1 (shown in Figure 1(b)) represent the relative position and width of the center ring in the reflector, respectively. Figures 8(a) and 8(b) show $|S_{11}|$and AR in the operating frequency rang with different G_3 and d_1. It can be

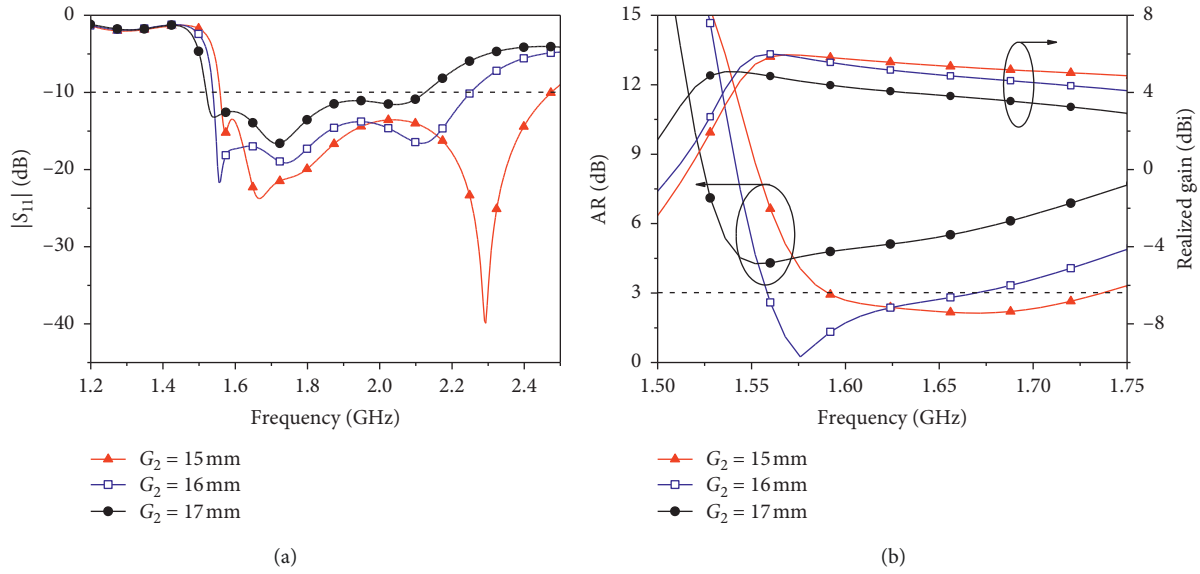

Figure 7: Variations of (a) $|S_{11}|$ and (b) AR and realized gain with different dimensions of the inner square patches, G_2.

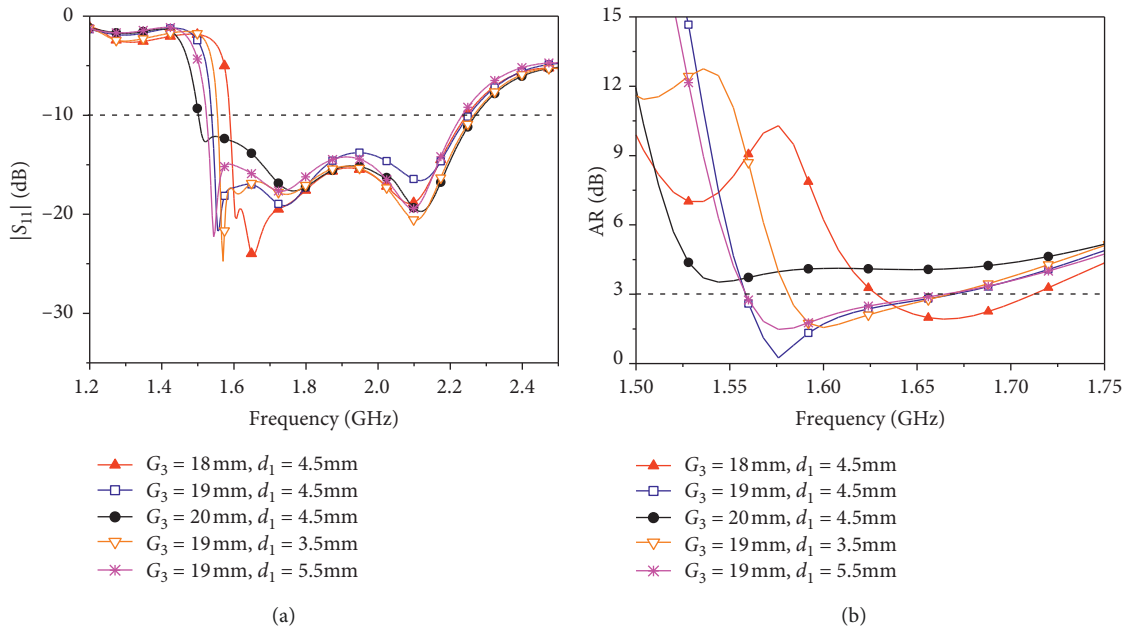

Figure 8: Variations of (a) $|S_{11}|$ and (b) AR with different dimensions of the center ring of the reflector, G_3 and d_1.

observed that $|S_{11}|$ has slight variations while AR has visible changes with the increase of G_3 from 18 mm to 20 mm and the increase of d_1 from 3.5 mm to 5.5 mm. This indicates that AR is more sensitive to the variation of the relative position and width of the center ring.

3.5. Dimensions of the Outer Ring of the Reflector (G_1 and G_4). $|S_{11}|$ and AR at the boresight of the proposed antenna with varying lengths of the outer ring of the reflector, G_1 and G_4, are computed, and the results are shown in Figures 9(a) and 9(b). When G_1 increases from 60.5 to 70.5 mm and G_4 increases from 24.5 mm to 26.5 mm, $|S_{11}|$ has slight variations while AR shows visible variations. The optimal values for small AR and antenna size are $G_1 = 65.5$ mm and $G_4 = 25.5$ mm.

Based on the above studies, the final geometrical parameters of the proposed antenna are listed in Table 1.

4. Experimental Results and Discussion

Based on the optimized parameters listed in Table 1, a prototype of the proposed antenna is fabricated, as shown in Figures 10(a)–10(c) for top, bottom, and side views, respectively, where the two layers are separated and supported with four plastic posts.

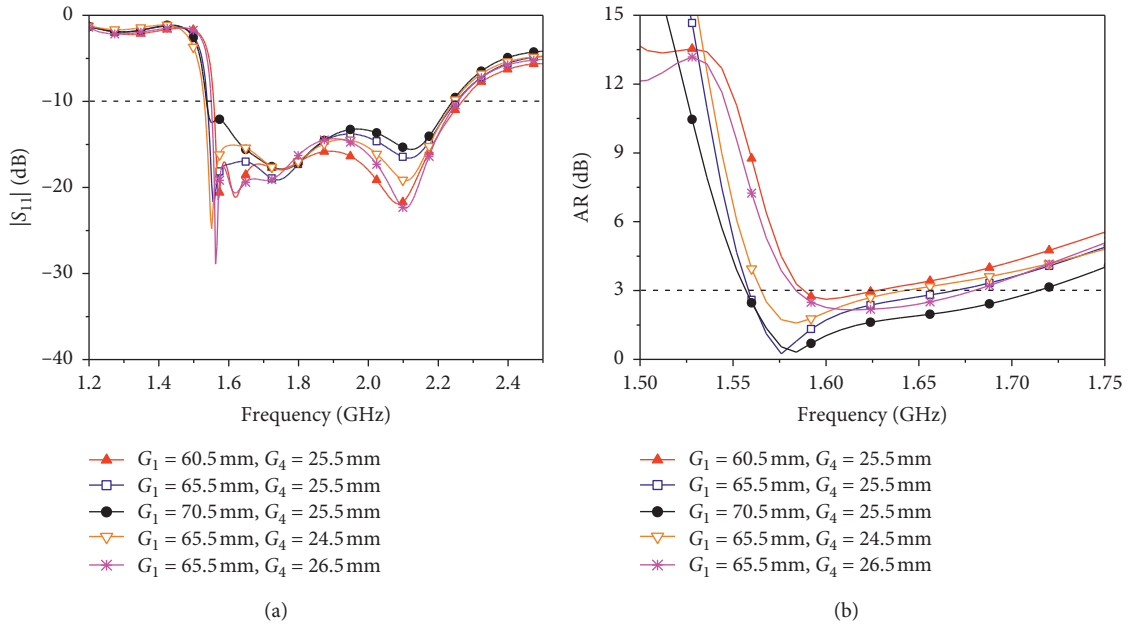

FIGURE 9: Variations of (a) $|S_{11}|$ and (b) AR with different dimensions of the outer ring of the reflector, G_1 and G_4.

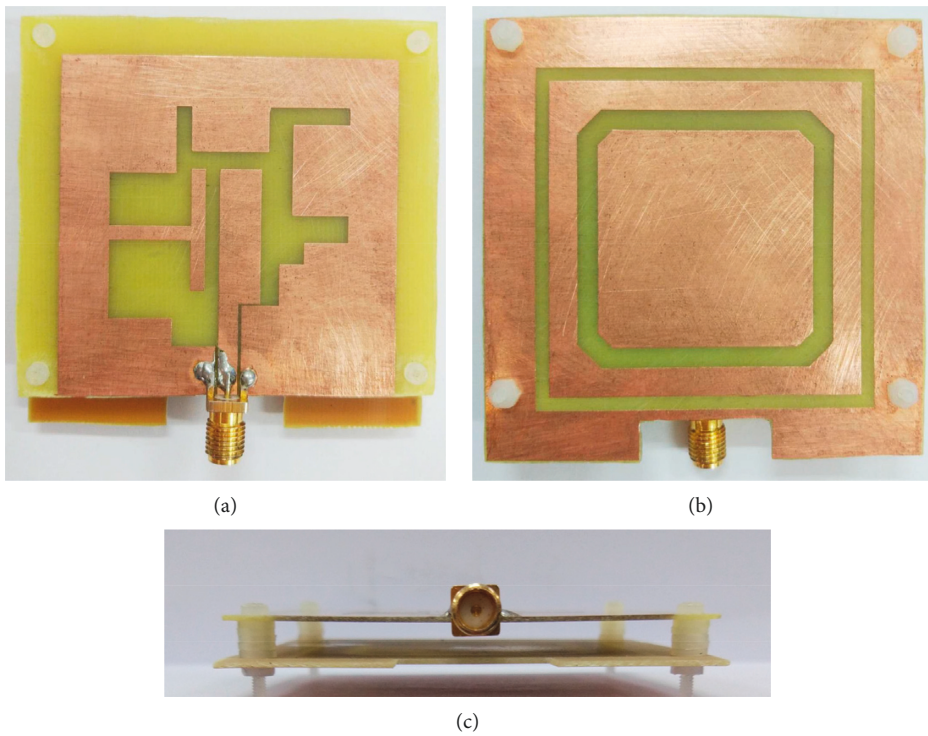

FIGURE 10: The fabricated prototype of the proposed antenna. (a) Top view, (b) bottom view, and (c) side view.

The prototype antenna was measured with Agilent E5071Cvector network analyzer for $|S_{11}|$ and for radiation pattern and AR in our anechoic chamber. The results are shown in Figure 11 It can be seen that the measured results agree reasonably well with the simulated ones. The measured $|S_{11}|$ frequency band of −10 dB is 1530 MHz to 2280 MHz which covers the full operating bandwidth of BD2 B_1, GPS L_1, and GLONASS L_1.

The simulated and measured AR and gain are shown in Figure 12(a). The measured 3 dB AR frequency ranges from 1558 MHz to 1672 MHz in RHCP. The measured results agree reasonably well with the simulated results. The

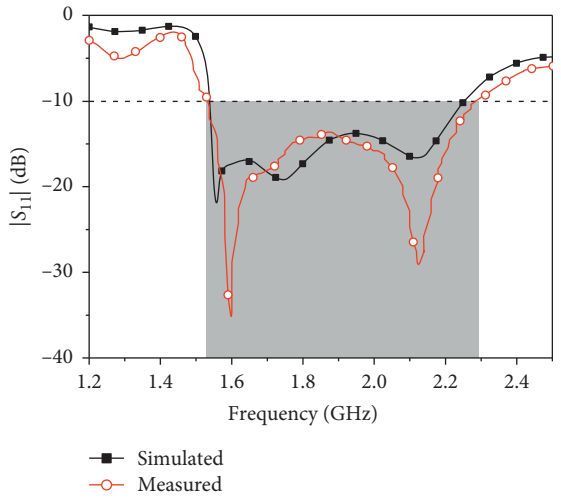

Figure 11: Simulated and measured $|S_{11}|$ of the proposed antenna.

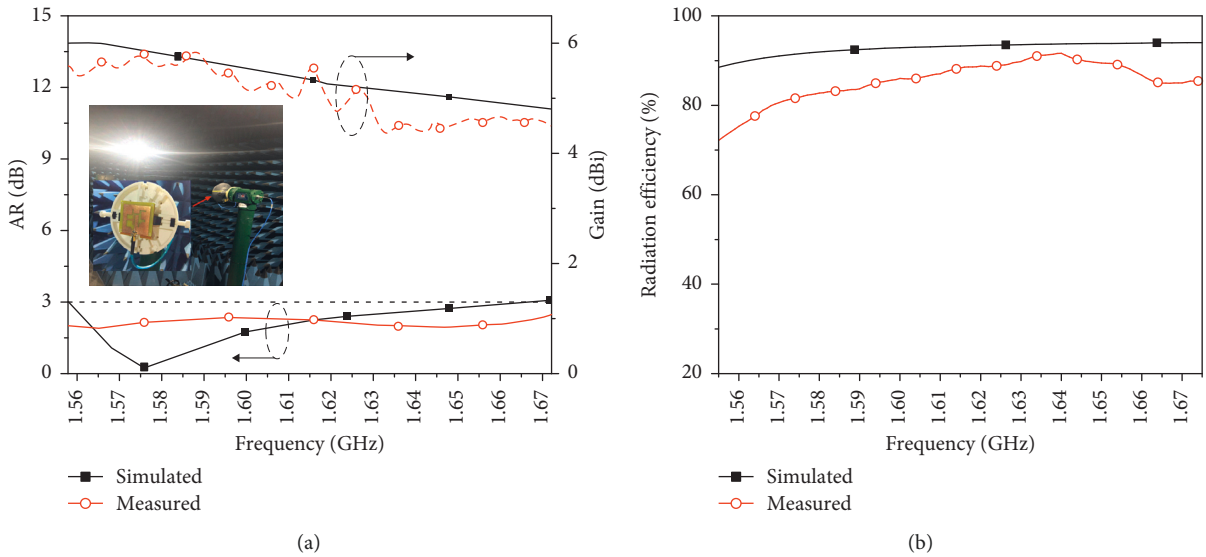

Figure 12: Measured and simulated results of (a) gain and AR at the boresight and (b) radiation efficiency.

measured gain varies with frequency and the gain is 5.26, 5.78, and 5.12 dBi at the center frequency of BD2 B_1 (1561 MHz), GPS L_1 (1575 MHz), and GLONASS L_1 (1602 MHz), respectively. The maximum measured gain is 5.87 dBi in the whole operating frequency band. The simulated and measured radiation efficiencies are shown in Figure 12(b). As can be seen, the measured radiation efficiencies are around 80%, while the simulated ones are around 90%. The discrepancy between simulations and measurements are mainly due to the errors of the conductivity of conductors and dielectric loss angle of tangent of the antenna between the theoretical values and the true values.

The normalized RHCP and LHCP radiation patterns of the proposed antenna at the frequency of 1.561, 1.575, and 1.602 GHz in the *xz* plane and *yz* plane are simulated and measured, respectively, and the results are shown in Figure 13. In all cases, the measured and simulated results have good corroborations.

Table 2 shows the comparison of the antenna size and performance between the proposed antenna and other recently published works. Here, we introduce the ratios of antenna volume size to relative bandwidth of $|S_{11}|$ and AR, RVB1, and RVB2, respectively; they are to measure the relative sizes of the antennas. Such ratio definitions for comparisons are justifiable and representative since the antenna size is proportional to the frequency it operates at. The smaller the ratio is, the better performance the antenna has in terms of the size.

As can be seen from Table 2, the proposed antenna has the smallest height of $0.033\lambda_0$ for profile and transverse area of $0.33 \times 0.33\ \lambda_0^2$, with the smaller ratio of 0.83 for RVB1 and 4.9 for RVB2. Therefore, it is the compact antenna with better performance of IBW and ARBW.

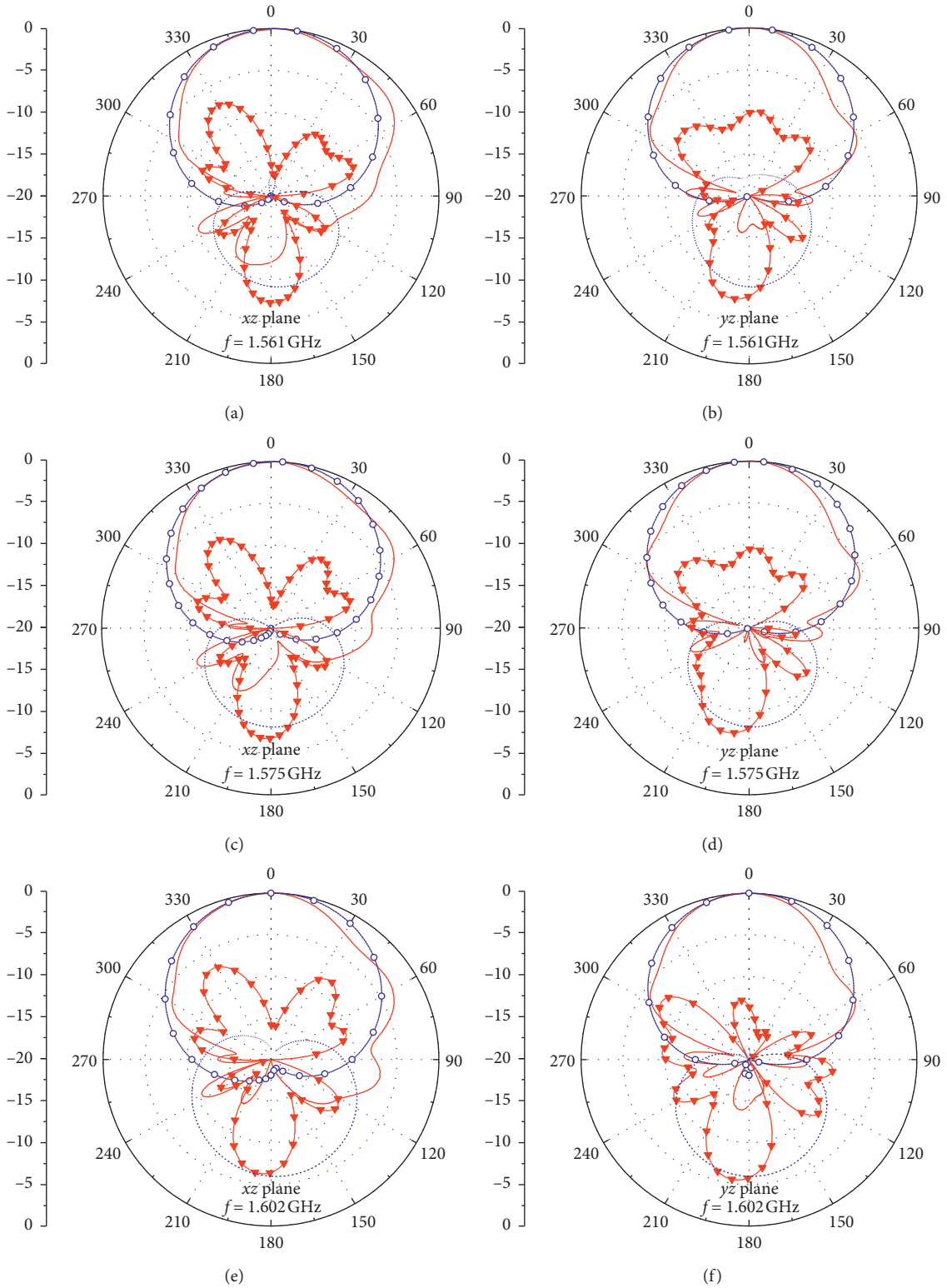

Figure 13: Simulated and measured radiation patterns in the *xz* plane and the *yz* plane at (a) $f = 1.561$ GHz, (b) $f = 1.575$ GHz, and (c) $f = 1.602$ GHz.

5. Conclusions

The CPW feed slot antenna is combined with the modified reflector to develop a new compact low-profile antenna with unidirectional radiation for GNSS application. The modified reflector contains an inner square patch with four slantly cut corners, a center ring, and an outer ring with a notch and has a small transverse area of $0.33 \times 0.33\ \lambda_0^2$. The proposed design can significantly reduce the separation gap between the radiator and the reflector and then result in a smaller

Table 2: Comparison of the antenna size and performance between this work and other recently published works.

Ref. no	Height (λ_0)	Area (λ_0^2)	IBW (%)	RVB1 ($\times 10^{-2}$)	ARBW (%)	RVB2 ($\times 10^{-2}$)
[4]	0.13	0.45×0.45	43.8	6.01	42.6	6.18
[5]	0.042	0.88×0.88	8.52	38.17	7	46.4
[6]	0.096	0.6×0.6	40.0	8.64	34.0	10.15
[7]	0.09	0.7×0.8	97.8	5.15	83.8	6.02
[15]	0.076	0.44×0.44	33.5	4.39	27.2	5.41
[16]	0.22	0.54×0.54	52.6	12.2	34.4	18.6
[17]	0.22	0.85×0.85	109.6	14.6	60.9	26.3
This work	0.033	0.3×0.3	41.8	0.83	7.1	4.9

Height = total profile height; area = area of the reflector; IBW = −10 dB $|S_{11}|$ relative BW; RVBR1 = ratio of antenna volume size to relative bandwidth of the $|S_{11}|$; ARBW = 3 dB AR relative BW; RVB2 = ratio of antenna volume size to relative bandwidth of the AR.

antenna profile of about $\lambda_0/30$. It has a wide IBW and ARBW of 41.8% and 7.1%, respectively, and meanwhile, the peak measured gain can reach 5.87 dBi in the whole operating frequency band. In addition, its structure is easily fabricated since it has a simple CPW feed and does not need additional feeding networks and shorting probes. It may also be used conveniently as an antenna array element because of its side-fed structure, low profile, and small size.

Data Availability

The data used to support the findings of this study are included within the article.

Conflicts of Interest

The authors declare that they have no conflicts of interest.

Acknowledgments

This work was supported by the Natural Science Foundation of Fujian Province of China under Grant no. 2019J01638 and the Science and Technology Project Plan of Fuzhou of China under Grant no. 2018-G-89.

References

[1] J. J. H. Wang, "Antennas for global navigation satellite system (GNSS)," *Proceedings of the IEEE*, vol. 100, no. 7, pp. 2349–2355, 2012.

[2] J. Yuan, J. Zheng, and Z. D. Chen, "A compact meandered ring antenna loaded with parasitic patches and a slotted ground for global navigation satellite systems," *IEEE Transactions on Antennas and Propagation*, vol. 66, no. 12, pp. 6835–6843, 2018.

[3] J. Wu, Y. Yin, Z. Wang, and R. Lian, "Broadband circularly polarized patch antenna with parasitic strips," *IEEE Antennas and Wireless Propagation Letters*, vol. 14, pp. 559–562, 2015.

[4] H. Zhang, Y. Guo, and G. Wang, "A wideband circularly polarized crossed-slot antenna with stable phase center," *IEEE Antennas and Wireless Propagation Letters*, vol. 18, no. 5, pp. 941–945, 2019.

[5] Q.-S. Wu, X. Zhang, and L. Zhu, "A feeding technique for wideband CP patch antenna based on 90° phase difference between tapped line and parallel coupled line," *IEEE Antennas and Wireless Propagation Letters*, vol. 18, no. 7, pp. 1468–1471, 2019.

[6] K. Luo, B. Chen, and W.-P. Ding, "Meander line coupled cavity-backed slot antenna for broadband circular polarization," *IEEE Antennas and Wireless Propagation Letters*, vol. 14, pp. 1215–1218, 2015.

[7] Q. Liu, Y. Li, Z. Mo, and Y. Liu, "Compact broadband circularly-polarized directional universal GNSS antenna with symmetric radiation pattern and stable near-zenith coverage," *IET Microwaves, Antennas & Propagation*, vol. 11, no. 5, pp. 657–663, 2017.

[8] L. Zhang, S. Gao, Q. Luo et al., "Single-feed ultra-wideband circularly polarized antenna with enhanced front-to-back ratio," *IEEE Transactions on Antennas and Propagation*, vol. 64, no. 1, pp. 355–360, 2016.

[9] C. Sun, Z. Wu, and B. Bai, "A novel compact wideband patch antenna for GNSS application," *IEEE Transactions on Antennas and Propagation*, vol. 65, no. 12, pp. 7334–7339, 2017.

[10] L. Wang, Z. Weng, Y.-C. Jiao, W. Zhang, and C. Zhang, "A low-profile broadband circularly polarized microstrip antenna with wide beamwidth," *IEEE Antennas and Wireless Propagation Letters*, vol. 17, no. 7, pp. 1213–1217, 2018.

[11] R. K. Saini and S. Dwari, "CPW-fed broadband circularly polarized rectangular slot antenna with l-shaped feed line and parasitic elements," *Microwave and Optical Technology Letters*, vol. 57, no. 8, pp. 1788–1794, 2015.

[12] P. Sadeghi, C. Ghobadi, and J. Nourinia, "Square slot antenna with two spiral slots loaded for broadband circular polarization," *Electronics Letters*, vol. 52, no. 10, pp. 787-788, 2016.

[13] M. S. Ellis, Z. Zhao, J. Wu, X. Ding, Z. Nie, and Q.-H. Liu, "A novel simple and compact microstrip-fed circularly polarized wide slot antenna with wide axial ratio bandwidth for C-band Applications," *IEEE Transactions on Antennas and Propagation*, vol. 64, no. 4, pp. 1552–1555, 2016.

[14] R. Xu, J.-Y. Li, J. Liu, S.-G. Zhou, Z.-J. Xing, and K. Wei, "A design of dual-wideband planar printed antenna for circular polarization diversity by combining slot and monopole modes," *IEEE Transactions on Antennas and Propagation*, vol. 66, no. 8, pp. 4326–4331, 2018.

[15] M. F. Farooqui and A. Kishk, "3-D-Printed tunable circularly polarized microstrip patch antenna," *IEEE Antennas and Wireless Propagation Letters*, vol. 18, no. 7, pp. 1429–1432, 2019.

[16] S. Pan, S. Jia-Yi, and T. Po-Jen, "Circularly polarized square slot antenna with a largely enhanced axial-ratio bandwidth," *IEEE Antennas and Wireless Propagation Letters*, vol. 11, pp. 969–972, 2012.

[17] G. Li, H. Zhai, L. Li, and L. Changhong, "A nesting-L slot antenna with enhanced circularly polarized bandwidth and radiation," *IEEE Antennas and Wireless Propagation Letters*, vol. 13, pp. 225–228, 2014.

[18] S. H. Yeung, K. F. Man, and W. S. Chan, "A bandwidth improved circular polarized slot antenna using a slot composed of multiple circular sectors," *IEEE Transactions on Antennas and Propagation*, vol. 59, no. 8, pp. 3065–3070, 2011.

[19] R. Xu, J.-Y. Li, K. Wei, and G.-W. Yang, "A broadband slot antenna with unidirectional circularly polarized radiation patterns," *IEEE Antennas and Wireless Propagation Letters*, vol. 16, pp. 317–320, 2017.